Lowland Technology International 2016; 17 (4): 215-224
International Association of Lowland Technology (IALT): ISSN 1344-9656

Research Paper

Experimental study on the effects of rainwater infiltration and cyclic loading on unsaturated silica sand

P.H.H. Giang [1], T. Uchimura [2], L.G. Lam [3] and W. Haegeman [4]

ARTICLE INFORMATION

Article history:

Received: 03 January, 2016
Received in revised form: 22 February, 2016
Accepted: 28 February, 2016
Published: March, 2016

Keywords:

Stiffness
Unsaturated soil
Cyclic loading
Water infiltration
Slope failure

ABSTRACT

This paper presents the result of cyclic loading tests followed by water infiltration on unsaturated sandy samples to study possible slope failures in earthquake areas. The cyclic tri-axial tests and dynamic measurements were carried out on Edosaki sand, silica sand taken from a natural slope in Chiba prefecture in Japan. The specimens were first consolidated in anisotropic condition with a principal stress ratio (K = 2), and then cyclically loaded under un-drained conditions. After cyclic loading, water infiltration was applied to the specimens until failure after different periods of waiting time. During the tests, the elastic wave velocities were continuously measured. Test results clearly show the variation of stiffness during cyclic loading and infiltration attributed to changes in relative density. Test results also confirm that there is a possible threshold value for the cyclic amplitude that causes a rearrangement of the soil skeleton and gives rise to higher failure resistance during water infiltration after reconsolidation. In short, it is very useful to monitor the stiffness and pore water pressure in a slope after an earthquake in areas with high and frequent rainfall.

1. Introduction

Slope failure is one of the most severe natural phenomena, which can occur in a short period of time, triggered by an intensive earthquake or heavy rainfall and causes a lot of damages to buildings, roads, embankments with many casualties. For example, on October 23rd, 2004, in an intensive earthquake (M. 6.8) in the Yamakoshi area, Mid Niigata Region, more than 65 people were killed, and several type of landslides were induced. On July 16th, 2007, the Chuetsu-Oki earthquake of magnitude 6.8 brought serious damages to the infrastructure and 11 people were killed by the collapse of the old houses in Kashiwazaki City, which is mostly flat and hilly areas on account of shallow landslides (Yamagishi et al. 2008). After an earthquake, shallow landslide may occur during rainfall. It is not easy to predict exactly for this case. At the moment, shallow landslides induced by a combination of earthquake and rainfall hasn't been considered in previous studies although there are many researchers who studied either on slope failure triggered by rainfall (Farooq, Orense, and Towhata, 2004; Fukuzono, 1987; Huang and Yuin, 2010; Tohari, et al., 2007) or on slope failure triggered by an earthquake (Chen, et al., 2009; Sassa, 2005; Tazawa, et al., 1988). Indeed, when an earthquake occurs, the

[1] Corresponding author, PhD candidate, Department of Civil Engineering, Ghent University, Technologiepark 905, B-9052 Zwijnaarde, BELGIUM, huuhagiang.pham@ugent.be
[2] Associate Professor, Department of Civil Engineering, The University of Tokyo, 7-3-1 Hongo, Bunkyo-ku, Tokyo, JAPAN, uchimura@geot.t.u-tokyo.ac.jp
[3] Lecturer & IALT member, Institute of Lowland Technology, Saga University, Saga 840-8502, JAPAN; Lecturer, Can Tho University, VIETNAM lglam@ctu.edu.vn
[4] Professor, Department of Civil Engineering, Ghent University, Technologiepark 905, B-9052 Zwijnaarde, BELGIUM, wim.haegeman@ugent.be
Note: Discussion on this paper is open until September 2016.

seismic loading on saturated soil and a rearrangement of the soil skeleton which both may lead to degradation in un-drained stiffness and strength expressed by a reduction in shear modulus G_{max} (Hardin and Richart, 1963 cited in Zhou & Chen, 2005). For unsaturated soils, the cyclic loading under un-drained condition causes the decreasing of effective stress due to the decreasing of matric suction (Nishimura, 2013). During rainwater infiltration into a shallow soil profile, initially in an unsaturated state, a reduction in suction occurs causing a drop in the effective normal stress acting along the potential failure plane and reduces the available shear strength (Anderson and Sitar N., 1995) shown in Fig. 1. Consequently the failure of the slope is primarily caused by a reduction in the matric suction. To study both effects of seismic loading and rainwater infiltration on slope stability, a piezoelectric – ceramic bender element measuring system was installed in a conventional tri-axial apparatus. Under un-drained cyclic loading and drained water infiltration conditions, a series of tests were carried out on Edosaki sand with measurement of compression and shear wave velocities (V_P and V_S) before and after cyclic loading and during water infiltration. In addition, after the cyclic loading and before the water infiltration, the effects of waiting time and the effect of relative density were also considered. Tests were conducted with different amplitude of cyclic loading but a constant water infiltration rate.

2. Test conditions

2.1 Material properties

All tests were performed on Edosaki sand taken from a natural slope in Chiba-Japan. The physical properties of Edosaki sand, determined according to the Japanese Geotechnical Society (JGS) standards, are summarized in Table 1 and the grain size distribution curve is shown in Fig. 2.

2.2 Initial stress conditions in the slope

Different methods for slope stability analysis are available to the engineers such as the limit analysis method, the limit equilibrium method, the finite element method or the finite differential method. However, almost engineers prefer to use the limit equilibrium method to analyze the slope stability. The 2D slice methods of limit equilibrium analysis have been studied by Fredlund (1984) and Duncan (1996) (Fig. 3). Based on these methods, Deng et al. (2010) proposed for seismic loading on the slope. The initial principal stresses can be calculated as the following equations:

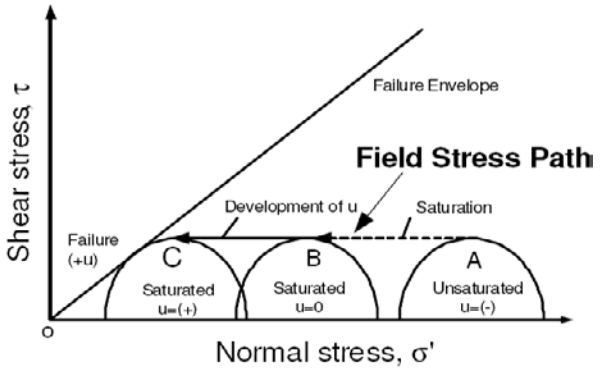

Fig. 2. Field stress path in a slope related to rainfall infiltration (Anderson and Sitar, 1995).

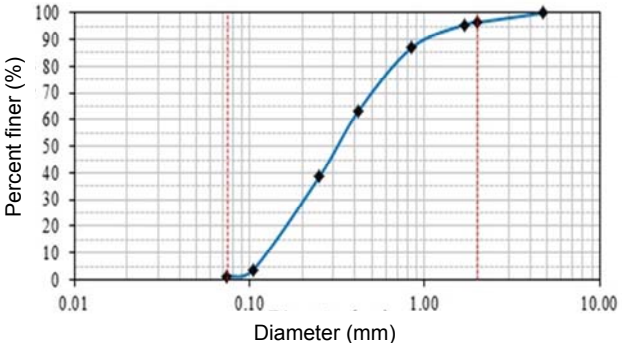

Fig. 1. Grain size distribution curve of Edosaki sand.

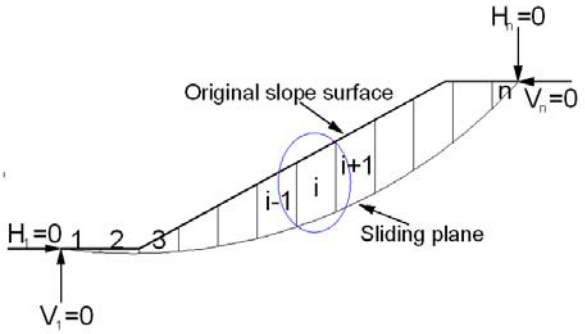

Fig. 3. 2D slice method with vertical slices.

$$\sigma_s^{'} = (\rho_s.g.z - \rho_w.g.H_w)((\cos\alpha)^2 - K_s.\sin\alpha.\cos\alpha) \quad [1]$$

$$\tau_s = (\rho_s.g.z)((\sin\alpha.\cos\alpha + K_s.(\cos\alpha)^2) \quad [2]$$

Assuming the inclination of shear band in tri-axial compression test is $\sigma_1'\ \sigma_3'$ (Fig. 4), is obtained based on the Mohr's stress circle (Fig. 5):

$$\sigma_3' = \sigma_s' - \frac{\tau_s}{\tan\theta} \quad [3]$$

$$\sigma_1' = \sigma_3' + \frac{2\tau_s}{\sin 2\theta} \quad [4]$$

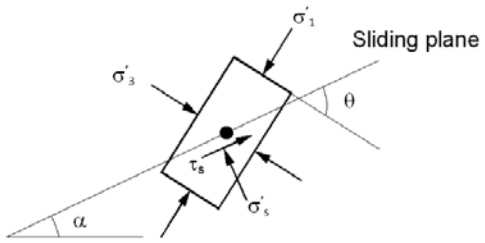

Fig. 4. In-situ stress state of undisturbed sample.

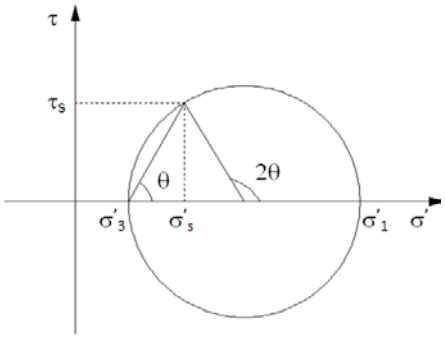

Fig. 5. Mohr's stress circle described in Fig. 4.

Table 1. Physical properties of Edosaki sand.

Parameters	Value
Specific gravity, G_s	2.686
Mean Grain size, D_{50} (mm)	0.32
Coefficient of Uniformity, $C_u = D_{60}/D_{10}$	2.92
Coefficient of Gradation, $C_c=(D_{30})^2/(D_{10}*D_{60})$	0.81
Sand content (%)	98.67
Fine content (%)	1.33
Maximum void ratio, e_{max}	1.683
Minimum void ratio, e_{min}	0.589
Max. dry density, $\rho_{d(max)}$ (g/cm^3)	1.687
Optimum water content, w_{opt} (%)	16.25

In this study, an element in the slope was assumed under the following conditions, to analyze the slope stability: α = 20°, ρ_s = 1.8g/cm^3, z = 1.65m, θ = 60°. The stresses for cyclic loading conditions applied in all the tests were, based on these parameters, set to σ_1 = 40kPa and σ_3 = 20kPa , and Δq_{amp} = 15kPa, Δq_{amp} = 20kPa for D_r = 40% and D_r = 70%, respectively.

3. Test apparatus

The combined tri-axial compression apparatus and dynamic measurement system was used in this study to perform all the cyclic loading and water infiltration tests for the investigation of stiffness changes.

3.1 Tri-axial compression apparatus

Cyclic load was applied by the axial loading system, controlled by a feedback system through an electro-pneumatic (E/P) transducer and D/A (digital-to-analog) converter. In order to measure the change in water content of the sample, a differential pressure transducer (DPT) used to measure the volume of water injection and an electric balance used to measure the volume of water ejection. Additionally, a linear variable differential transducer (LVDT) was fixed on a metal bar attached to the upper horizontal frame and a clip gauge at the middle of specimen to monitor the axial deformation and the changes of the specimen's diameter. Figure 6 shows the scheme of the tri-axial compression apparatus. It is worth to mention that the present set-up did not allow for the measurement of suction during testing since no high air-entry ceramic disk was used at the bottom of the soil specimen.

3.2 Dynamic measurement system

In this study, a function generator was used to generate P and S waves. In order to amplify the input voltage from the function generator to the bender element and piezoelectric ceramic, a signal amplifier was used as shown in Fig. 7. Furthermore, a buffer amplifier was applied to reduce the electro-magnetic noise during testing. The waveform measuring system is a multi-unit compliant data acquisition system, with high-speed analog voltage measurement unit so signals can be

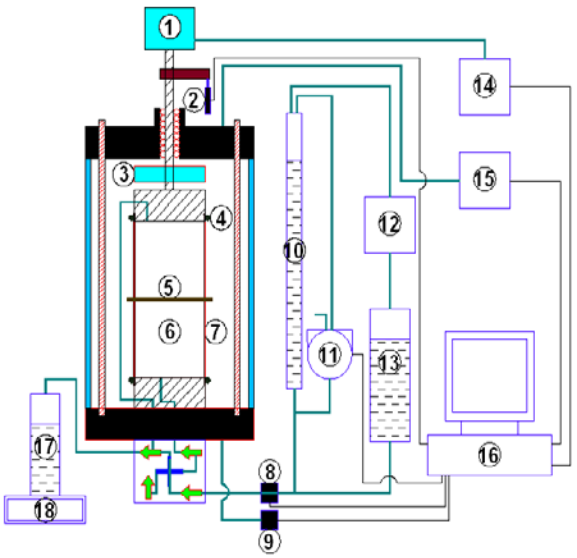

Fig. 6. Scheme of the tri-axial compression apparatus.
1.Bellofram cylinder, 2.LVDT, 3.Load cell, 4.O-ring, 5.Clip gauge, 6.Specimen, 7.Membrance, 8.Pore water pressure transducer, 9.Cell pressure transducer, 10.Burette, 11.DPT, 12. Air pressure, 13.Water supply, 14.E/P-Axial load control, 15.E/P-Cell pressure control, 16.Computer, 17.Drained water, 18.Electric balance.

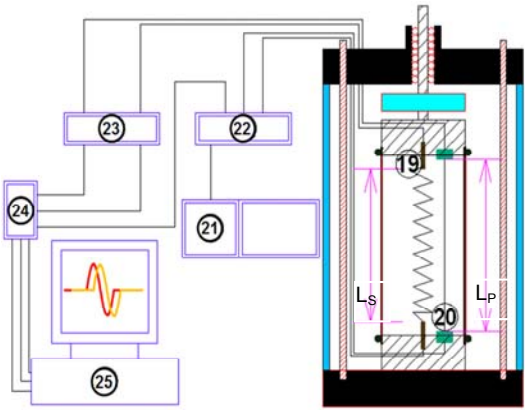

Fig. 7. Scheme of dynamic measurement system. 19.Bender elements, 20.Piezoelectric ceramic elements, 21. Function generator, 22.Signal Amplifier, 23. Buffer amplifier, 24.Wave logger, 25. Computer.

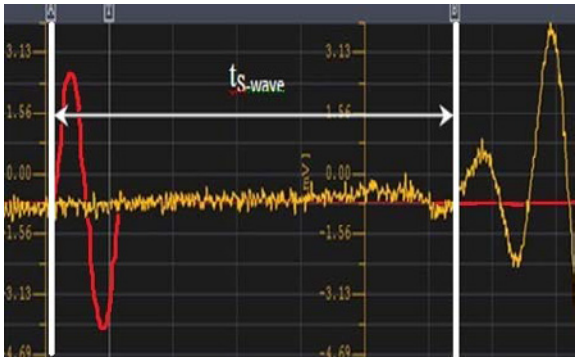

Fig. 8. Typical bender element record (S wave).

obtained.

3.3 Stiffness measurement

The bender element method is originally developed by Shirley and Hampton in 1978 as cited by Lee and Santamarina (2005) to obtain the shear modulus (G_{max}) of a soil by measuring the velocity of shear wave (S-wave) propagating through a sample. This method has generated intensive studies from many researchers in the past (Bellotti et al. 1996; Builes et al. 2008; Santamarina and Fratta 2005; Karg and Haegeman 2009). In addition, by using piezoelectric ceramic element measuring the velocity of the primary wave (P-wave), the constrained modulus *M* is obtained. The S wave and P wave velocity V_S and V_P in the specimen can be calculated from the wave travel time *t* and the known separation *L* between the two bender elements or piezoelectric ceramic elements. According to ASTM D2845, the wave travel time is calculated out of the first arrival signal (Kumar and Madhusudhan 2010; Viggiani and Atkinson 1995) as shown in Fig. 8. The travel time *t* is computed based on time between the first rising point of the input and the first rising point of output signals. With this technique, t_P is clearly identified. Identification of t_S however is more demanding since near field effects occur when the degree of saturation S_r exceeds about 80 %. To reduce noise in the signals, a stacking technique used in Santamarina and Fratta (2005) and Brandenberg et al. (2008) was applied. Therein, a prescribed number of output wave signals were recorded and averaged before identification of the travel time.

By monitoring the density of the specimen during testing and measuring the travel time hence wave velocity, the soil stiffness modulus can be obtained. Since primary (P) and secondary wave velocities (S) have been assessed, both constrained and shear modulus can be calculated as follows:

$$M = \rho_s \cdot V_P^2 \quad [5]$$

$$G = \rho_s \cdot V_S^2 \quad [6]$$

$$E = \frac{M\ (1-2\nu)(1+\nu)}{1-\nu} \quad [7]$$

where shear velocity $V_S = \frac{L}{t_S}$, compression velocity $V_P = \frac{L}{t_P}$, Poisson's ratio $\nu = \frac{0.5V_P^2 - V_S^2}{V_P^2 - V_S^2}$

4. Test Procedures

4.1 Sample preparation

The diameter and height of the cylinder specimens in all the tests were 10 cm and 20 cm respectively. Edosaki sand was first dried in the oven during one day, and then passed through the 2 mm sieve to remove the larger particles. The oven-dry sand was weighed and divided into 10 equal portions. For each portion, de-aired water was added to mix to wet sand with an initial water content of 10 %. The cylindrical two split mold was placed on the pedestal and the rubber membrane (0.3 mm thickness), which was tightened to the circumference of the pedestal by an O-ring, was stretched tight to the inside face of the split mold. A paper filter was placed on the pedestal of the specimen, and then the wet sand was tamped in 10 layers of the same height (2 cm) until the height of the specimen was reached. Finally, after the specimen was set up by stretching up and tightening the membrane to the top cap, a vacuum of 10 kPa was applied and the split mold was removed. This wet tamping technique proposed by Ladd (1978) and used in the researches (Farooq et al. 2004; Silver 1980; Guo and Wang 2009) has the benefit of controlling the water content with a target dry density.

4.2 Consolidation of the specimen

Before consolidation of the specimen, the acrylic cell was placed on the base plate of the tri-axial cell and was clamped tightly with the top plate in order to avoid any leakage of the cell pressure. Then, the cables of the dynamic measurement system, the clip gauge, LVDT and the load cell were connected to the computer. First, the specimen was consolidated under anisotropic stress condition increasing the stresses with a rate of 0.2 kPa/sec to a confining pressure σ_3 of 20 kPa and the specified value of principal stress ratio $K = \sigma_1/\sigma_3 = 40/20 = 2$. After setting up the data save time to 2 s, consolidation was allowed running until the axial and radial strain achieve a constant value.

4.3 Testing

After consolidation of the specimen, there are two samples first were performed to identify the maximum deviator stress (q) under monotonic loading to get the peak values of the axial stress for different initial relative density (D_r). These values are used to determine the cyclic loading amplitude, Δq_{amp}, for each relative density. The monotonic loading rate was set up to 0.5 kPa/min. The process was finished when approaching 15 % of axial strain. Figure 9 shows that the value of Δq_{max} is found within a range of $0 < \varepsilon_a \leq 15$ %, for $D_r = 40\%$, the value of Δq_{max40} equals 32.5kPa at ε_a=15 %; for D_r = 70 %, Δq_{max70} is 63kPa (ε_a=14,5 %).

To simulate the field stress path of a soil element along the potential failure plane, a cyclic loading followed by a water infiltration at low rate was applied to the specimen to observe the soil failure during the wetting process (Anderson and Sitar N., 1995). As shown in Fig. 10, there are three test sequences in this study, the first sequence (without cyclic loading) was water injection until failure, the second was water injection immediately after cyclic loading, and the last was first cyclic loading applied and then water injection supplied after a waiting period.

The cyclic loading was applied under un-drained condition. Five cycles were applied with a stress rate of 5kPa/min. Since the drainage valve was opened after the cyclic loading, drainage was possible during the waiting period and the water infiltration process. The dynamic measurement tests were performed after initial consolidation and during all sequences of the laboratory test. As noted in Fig. 10, during the waiting period, the specimens were re-consolidated under the same stress condition as in the initial consolidation process (σ_1/σ_3= 40/20). During this waiting period, the dynamic measurement tests were performed 6 hrs, 12 hrs, 18 hrs,

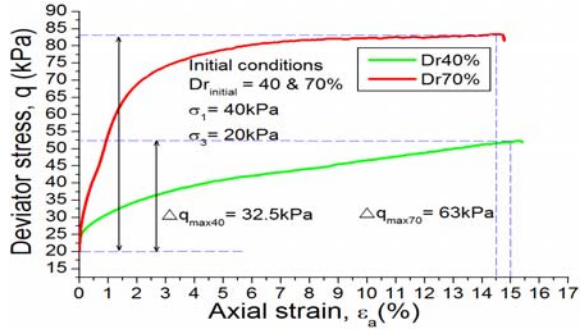

Fig. 9. Amplitude of cyclic loading (Δq_{max}) decided by monotonic loading tests.

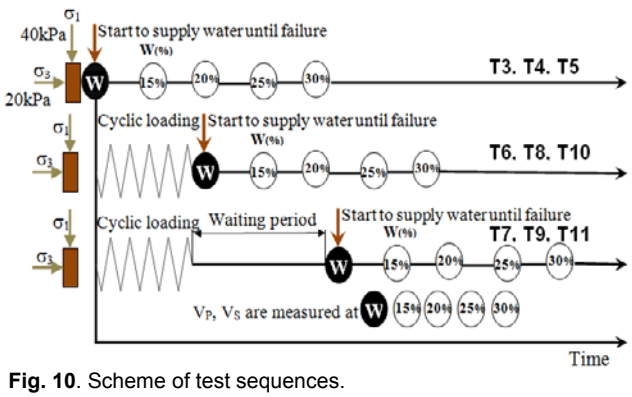

Fig. 10. Scheme of test sequences.

1 day, 2 days, 3 days after cyclic loading. Water injection only started when the value of the stiffness modulus was constant. Then the water injection with a constant rate of 1.5 ml/min was applied and decreases suction and effective stresses under constant total stresses until the specimen fails. Meanwhile, dynamic measurement tests were performed at 10 %, 15 %, 20 %, 25 %, and 30 % of water content.

The test conditions such as relative densities D_r before and after consolidation, amplitude of cyclic loading Δq_{amp}, and waiting period, t, for all tests are summarized in Table 2. For example, T3: WTCL-18h-40 was a specimen with initial D_r = 40 % and tested without cyclic loading and 18 hours waiting period before supplying water.

5. Test Results and Discussions

The relationship between axial strain and elapsed time from all of the test results are shown in Fig. 11. Out of all dynamic tests performed a linear relationship is revealed between Young's modulus E and shear modulus G_{max} as shown in Fig. 12, leading to Poisson's ratio of 0.35. Therefore, in the following discussion is focused on the shear modulus G_{max}.

Table 2. Test conditions.

Name of test	$D_{r\,initial}$ (%)	$D_{r\,after\,con.}$ (%)	Amplitude of cyclic loading Δq_{amp} (kPa)	Waiting period t (h)
T1: ML40	40	48.4	-	-
T2: ML70	70	71.1	-	-
T3: WTCL-18h-40	40	48.6	0	18
T4: WTCL-3days-40	40	48.9	0	72
T5: WTCL-0h-70	70	71.4	0	0
T6: 15kPa-0h-40	40	47.5	±15	0
T7: 15kPa-18h-40	40	48.1	±15	18
T8: 20kPa-0h-40	40	48.5	±20	0
T9: 20kPa-3days-40	40	49.2	±20	72
T10: 20kPa-0h-70	70	71.8	±20	0
T11: 20kPa-12h-70	70	71.5	±20	12

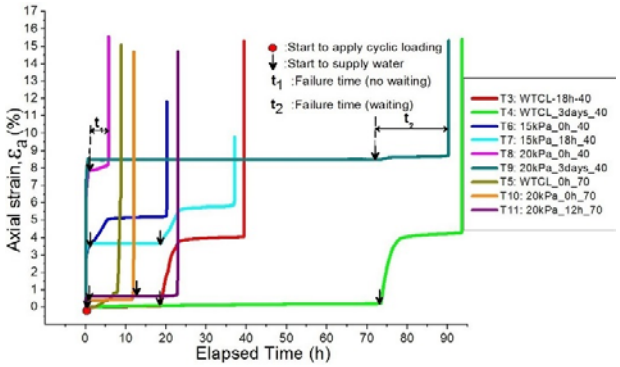

Fig. 11. Axial strain versus elapsed time.

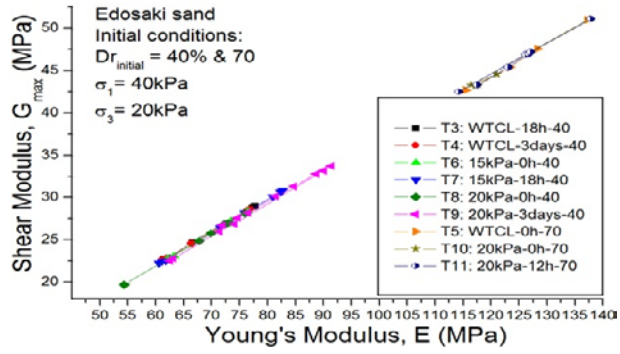

Fig. 12. Relationship between shear modulus and Young's modulus (D_r = 40% & 70%).

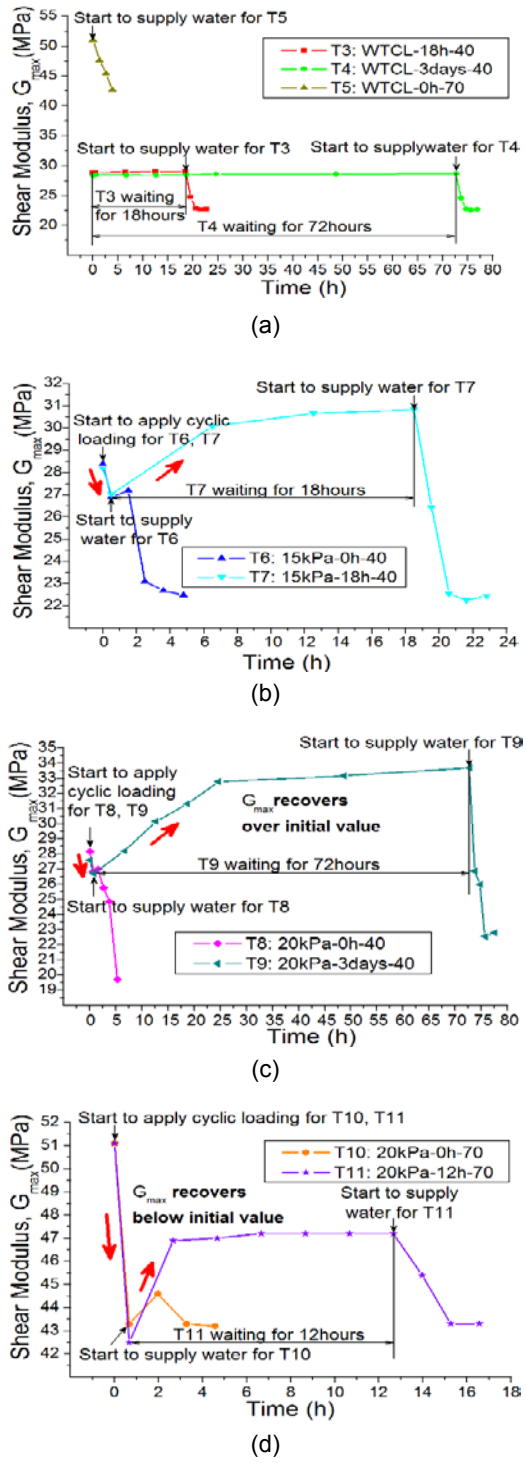

Fig. 13. Measurement of shear modulus versus time.

5.1 Stiffness measurements

Figures 13 show the measurement of the shear modulus versus time for tests T3 till T11. First of all, there is no significant difference in stiffness between the specimen T3 and the specimen T4 tested with consolidation time difference. It also can be seen that at the end of consolidation the shear modulus of samples T5, T10, and T11 are higher due to the higher compaction degree. During the cyclic loading all samples show a drop in shear modulus. This decrease is caused by a drop in effective stress due to a decrease of the suction during loading and is significantly higher for the well compacted sand samples T10 and T11. However during the waiting time and reconsolidation of the samples T7, T9 and T11 the shear modulus increases

again to a constant value. The shear modulus at the end of the waiting period for the samples T7 and T9 is higher than the shear modulus at the end of primary consolidation. This is due to a compaction and rearrangement of the particles during the cyclic loading and waiting period of this medium compacted sand. On the other hand, in sample T11 a lower shear modulus is found at the end of the waiting time due to dilatancy of the well compacted sample during cyclic loading. The cyclic loading amplitude in these tests has less influence on the decrease and increase of the shear modulus if we compare test results T7 and T9. For the samples compacted during loading it takes more time for the recovery of the shear modulus than for the dilated sample.

Water infiltration in all cases reduces the shear stiffness to due reduction in effective stresses. However a small increase in shear modulus is seen when infiltrating the water just after the cyclic loading. It is believed that in this case the flushing interferes with the reconsolidation of the sample hence the variation in pore water pressures, particle rearrangement and compaction hence causing an increase in stiffness.

5.2 Failure time during water infiltration

Figure 14 shows the axial strain versus the elapsed time for tests T3 till T11. A steep rise of axial strain introduces the failure of the sample.

In this figure it can be seen that a gradual increase in cyclic amplitude from 0kPa over 15 kPa to 20 kPa reduces the time to failure if the sample is percolated immediately after cyclic loading. This is due to the higher reduction in effective stresses during cyclic loading at higher cyclic amplitudes. This reduction is continued during water infiltration and so reducing the shear strength until failure.

It can also be seen in Figs. 14a and 14b that there is no significant difference in failure time, which corresponds to the amount of water injection, between the specimen T6 ($t_{failure6}$ = 20 hours) tested without waiting time and the specimen T7 ($t_{failure7}$ = 19 hours) tested after 18 hours waiting time, both tested under the same cyclic loading amplitude (Δq_{amp} = ±15 kPa). A similar tendency is observed between the specimens T3 and T4 after 18 hours and 3 days waiting time respectively (Fig. 14a).

However, T9, the test done under larger amplitude of cyclic loading (Δq_{amp} = ±20kPa) and 3 days waiting time took 17.5 hours to collapse, significantly longer than in the test T8 without waiting time ($t_{failure8}$ = 5 hours). These test results are shown in Fig. 14c. Finally, again no difference is noticed in time to failure for the tests at higher initial relative density (70%) and cyclic loading amplitude 20kPa (see Figs. 14a and 14d).

In this way it is shown that there is a threshold value for the cyclic amplitude, depending on the relative density of the soil material, causing a rearrangement of the soil skeleton giving rise to higher failure resistance during water infiltration after reconsolidation.

5.3 Saturation degree

A key factor in rainfall induced landslides is the compaction degree of the subsurface soil. Therefore, the effect of saturation degree during water infiltration is studied some more.

Figures 15 show the results of axial strain and saturation degree in function of time at both tested relative densities and different waiting periods before water infiltration. For both densities considered, small axial strains were measured during the initial phase of water infiltration. However, after a certain time axial strain starts to develop suddenly. This point is identified as the failure initiation of the soil sample. Once failure initiation is reached the development of axial strain progresses rapidly and large axial strains are reached in a short period of time. It can be noted that the initiation of failure takes place almost at the same overall degree of saturation, calculated based on the volume of water that flowed in and out of the sample, independent of the initial relative density, cyclic loading amplitude or reconsolidation period. This overall degree of saturation at failure initiation ranged from 79-82 % except for T8 (77 %) showed in Fig. 15d, indicating that failure was initiated in specimens that were not fully saturated.

As mentioned earlier, water was infiltrated into the specimen with a constant rate of 1.5 ml/min causing the same rate of saturation independent of the initial relative density. All samples took about five hours to approach the saturation value at failure initiation; however in almost all samples, except for T8, it took several hours more, with slightly increasing degree of saturation, to reach the transition point with failure initiation.

The tests presented in Figs. 15 show that the axial strain time history of specimens subjected to water infiltration can be divided in three parts. During increase of saturation degree axial strains are increasing, when approaching the degree of saturation at failure the rate of strain development decreases and finally dramatically increases again at failure initiation. A possible explanation for this deformation response is that during the initial phase of infiltration and saturation, bonds between the grains are broken as water permeates through the pores, resulting in continuous deformation.

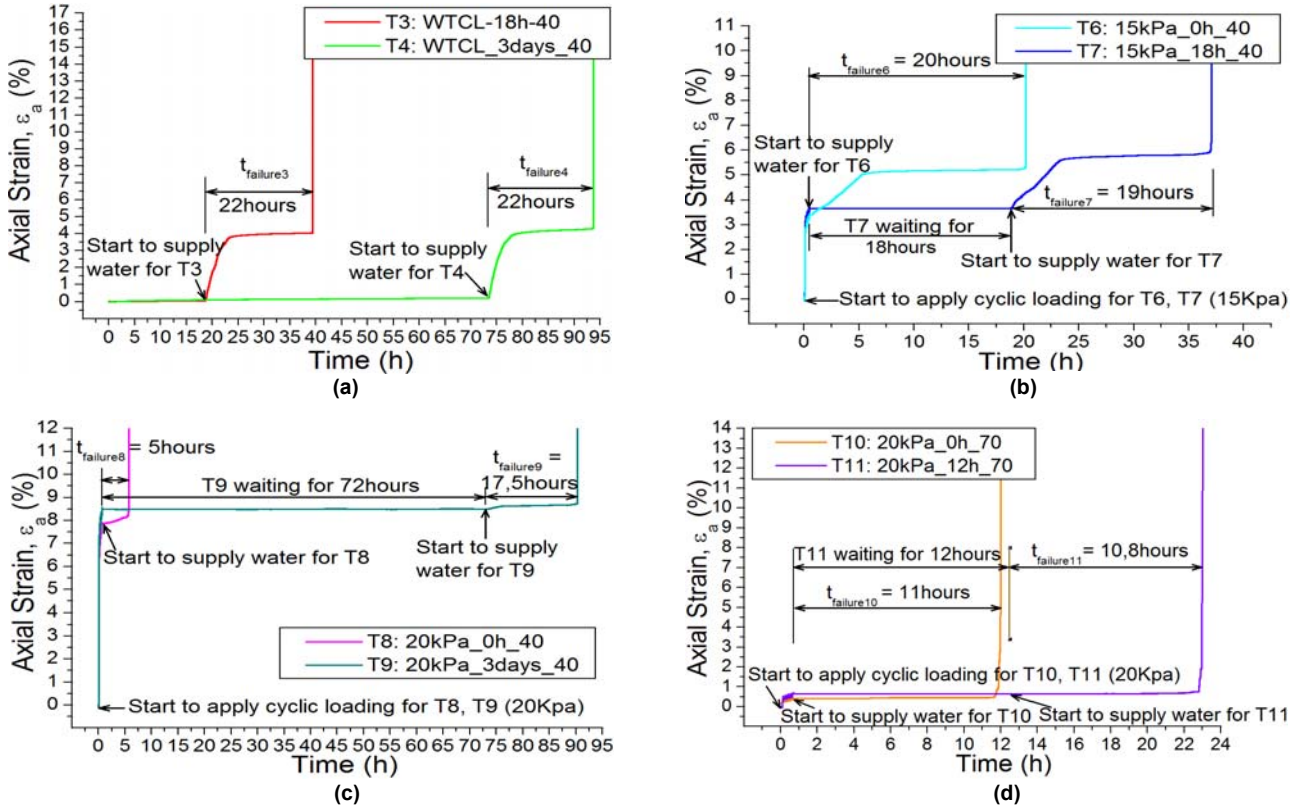

Fig. 14. Axial strain versus elapsed time.

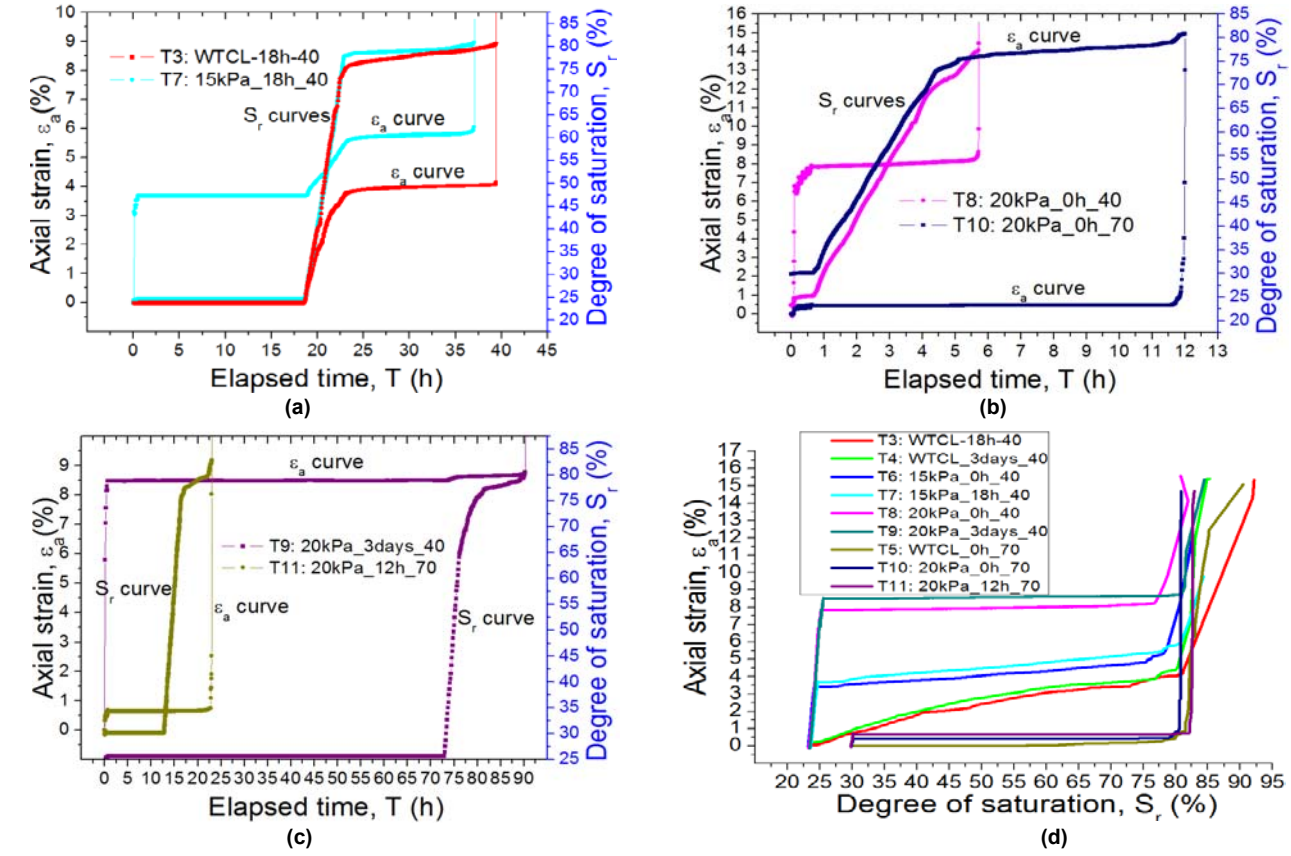

Fig. 15. Axial strain and saturation time histories.

However after some time, all weaker bonds are destroyed and pore pressure redistribution occurs with smaller accompanying deformation, also already noted by Farooq et al. (2004). Finally sufficient pore water pressure develops within the sample to decrease the shear strength initiating failure. Bonding between grains, so structural formation, and pore pressure redistribution obviously depends on prior cyclic loading and reconsolidation period, possibly explaining why at lower relative densities (40 %), higher cyclic amplitudes (20 kPa) and no reconsolidation (0 h) sample T8 immediately fails when above mentioned saturation degree is reached.

In the same reasoning denser compacted samples fail faster than less compacted samples during water infiltration since pore pressure redistribution and pore water pressure build up occurs faster due to a higher void ratio.

The rate of strain development during saturation decreases as the relative density increases (T9 = 0.000779 %/min and T11 = 0.000045 %/min) and the cyclic amplitude during prior loading increases (T3 = 0.014254 %/min, T7 = 0.006879 %/min and T9 = 0.000779 %/min). Such behavior implies that looser deposits may undergo more rapid movement compared to denser soils during water infiltration unless prior densified by an earthquake

6. Conclusions

Under un-drained cyclic loading and drained water infiltration conditions, a series of tests was carried out on Edosaki sand with measurement of wave velocities (V_P and V_S) to study the development of rainfall-induced slope failure after earthquake loading. In addition, the effects of waiting time after the cyclic loading, before the infiltration and the effect of relative density were also considered. Tests were conducted with different amplitude of cyclic loading but constant water infiltration rate. Based on the test results the following conclusions can be drawn:

- Cyclic loading reduces the stiffness of the unsaturated soil. This stiffness is recovered during the reconsolidation period giving rise to higher or lower shear moduli in comparison to the initial stiffness, depending on the relative density and cyclic loading amplitude.
- Water infiltration significantly reduces the shear stiffness of the material. In all samples shear stiffness at failure (due to water infiltration) seems not to be influenced by the waiting period, hence reconsolidation of the specimen.
- Initiation of failure takes place almost at the same overall degree of saturation, independent of the initial relative density, cyclic loading amplitude or reconsolidation period.
- The rate of strain development during saturation decreases as the relative density increases and the cyclic amplitude during prior loading increases suggesting that looser deposits may undergo more rapid movement compared to denser soils during water infiltration unless prior densified by an earthquake.
- There is a possible threshold value for the cyclic amplitude, depending on the relative density of the soil material, causing a rearrangement of the soil skeleton giving rise to higher failure resistance during water infiltration after reconsolidation.

These results may be useful for comparison between laboratory and in situ tests monitoring the stiffness and pore pressures in slopes to predict rainfall-induced failures after the earthquake.

Acknowledgement

The authors would like to express their gratitude to Prof. Ikuo Towhata and Prof. Junichi Koseki at The University of Tokyo for their valuable suggestions and comments in this study, and thank Dr. Suguru Yamada for his kind help in conducting part of the laboratory tests.

References

Anderson, S. A. and Sitar, N. , 1995. Analysis of rainfall-induced debris flows. Geotechnical Engineering, **121** (7): 544–552.

Bellotti, R., Jamiolkowski, M., Presti, D. C. F. Lo and O'Neill, D. A., 1996. Anisotropy of small strain stiffness in Ticino sand. Geotechnique, **46** (1): 115–131.

Brandenberg, S. J., Kutter, B. L. and Wilson, D. W., 2008. Fast stacking and phase corrections of shear wave signals in a noisy environment. Geotechnical and Geoenvironmental Engineering, **134** (8): 1154–1165.

Builes, M., García, E., and Riveros, C., 2008. Dynamic and static measurements of small strain moduli of toyoura sand. Revista Facultad de Ingeniería Universidad de Antioquia, **43**: 86–101.

Chen, X., Kato, N., Tsunaki, R. and Mukai, K., 2009. Prediction of slope failure due to earthquake. Chinese Science Bulletin, **54** (16): 2888–2894.

Deng, J., Tsutsumi, Y., Kameya, H. and Koseki, J., 2010. A modified procedure to evaluate earthquake-induced displacement of slopes containing a weak layer. Soils and Foundations, **50** (3): 413–420.

Duncan, M., 1996. State of the art: limit equilibrium and finite-element analysis of slopes. Geotechnical Engineering, **122** (7): 577–596.

Farooq, K., Orense, R., and Towhata, I., 2004. Response of unsaturated sandy soils under constant shear stress drained condition. Soils and Foundations, **44** (2): 1–13.

Fredlund, D. G., 1984. Analytical methods for slope stability analysis. Proc. 4th International Symposium on Landslides, September 16-21, Toronto, Canada: 229-250.

Fukuzono, T., 1987. Experimental study of slope failure caused by heavy rainfall. Proc. Corvallis Symposium, August 3-7, Oregon, USA, **165**: 133–134.

Guo, Y. and Wang, Y., 2009. Experimental study about the influence of initial water content in wet tamping method on static triaxial test results of silt. Electronic Journal of Geotechnical Engineering, **14**: 1–13.

Huang, C.-C. and Yuin, S.-C., 2010. Experimental investigation of rainfall criteria for shallow slope failures. Geomorphology, **120** (3-4): 326–338.

Karg, C. and Haegeman, W., 2009. Elasto-plastic long-term behavior of granular soils: Experimental investigation. Soil Dynamics and Earthquake Engineering, **29** (1): 155–172.

Kumar, J. and Madhusudhan, B. N., 2010. A note on the measurement of travel times using bender and extender elements. Soil Dynamics and Earthquake Engineering, **30** (7): 630–634.

Ladd, R. S., 1978. Preparing test specimen using undercompaction. Geotechnical Testing Journal, **1** (1): 16–23.

Lee, J. S., and Santamarina, J. C., 2005. Bender elements: Performance and signal interpretation. Geotechnical and Geoenvironmental Engineering, **131** (9): 1063–1070.

Nishimura, T., 2013. Evaluation of effective stress of an unsaturated soil under cyclic loading. Earthquake-Induced Landslides, Springer: 537-546.

Santamarina, J. C. and Fratta, D., 2005. Discrete signals and inverse problems: An introduction for engineers and scientists. John Wiley & Sons.

Sassa, K., 2005. Landslide disasters triggered by the 2004 Mid-Niigata Prefecture earthquake in Japan. Landslides, Springer, **2** (2): 135–142.

Silver, M.L., Tatsuoka, F., Phukunhaphan, A. and Avramidis, A.S., 1980. Cyclic undrained strength of sand by triaxial test and simple shear test. Proc. 7th World Conference on Earthquake Engineering, Istanbul, Turkey, **3**: 281-288 .

Tazawa, S., Yui, Y. and Kuribayashi, E., 1988. Probability of slope failures caused by earthquakes. Proc. 9th World Conference on Earthquake Engineering, August 2-9, Tokyo-Kyoto, Japan **3**: 145–150.

Tohari, A., Nishigaki, M. and Komatsu, M., 2007. Laboratory rainfall-induced slope failure with moisture content measurement. Geotechnical and Geoenvironmental Engineering, **133** (5): 575–587.

Viggiani, G. and Atkinson, J., 1995. Interpretation of bender element tests. Geotechnique, **45**(1): 149–154.

Yamagishi, H., Iwahashi, J. and Ayalew, L., 2008. GIS Using Landslide Mapping in Niigata Region , Japan. In The 1st Landslide Forum, November 20, Tokyo, Japan: 366–369.

Zhou, Y. and Chen, Y., 2005. Influence of seismic cyclic loading history on small strain shear modulus of saturated sands. Soil Dynamics and Earthquake Engineering, **25** (5): 341–353.

Symbols and abbreviations

α	Slope angle of the base
θ	Inclination angle of shear band
τ_s	Shear stress
σ'_s	Effective stress
σ_1	Major normal stress in tri-axial compression test
σ_3	Minor normal stress in tri-axial compression test
q	Deviator stress
Δq_{amp}	Cyclic loading amplitude
K_s	Seismic coefficient
ρ_s	Density of soil
ρ_w	Density of water
g	Gravity of earth (g=9.80665 m/s^2)
z	Height of block
H_w	Distance between ground water level & sliding plane
E	Young's modulus
G_{max}	Shear modulus
M	Constrained modulus
V_P	P - wave velocity
V_S	S - wave velocity
t	Travel time
L	Distance between bender elements or piezoelectric ceramic elements